Chapter 4:

Understanding the *In Situ* Mechanistic Control of Plant-Derived Carbon Quantum Dots on the Synthesis of Gold Nanoparticles

4.1 Introduction

4.1.1 Brief Introduction to Gold Nanopaticles

Gold nanoparticles (AuNPs) have proven to be an indispensable tool in nanotechnology owing to easy calorimetric assays and high extinction cross-section in the visible wavelength region. The underlying reason for this phenomenon is the collective oscillations of free electrons, known as localized surface plasmon resonance (LSPR), exploited extensively in recent years due to easy synthesis and surface functionalisation of AuNPs.[1] Mie theoretically elucidated upon this phenomenon by ascribing the plasmon band to the dipole oscillations of free electrons situated in the conduction band above Fermi energy level.[2] AuNPs can be found in morphologically diverse forms like nanospheres, nanocages, nanostars, nanoprisms, nanocubes, nanorods/nanowires, nanodisks and nanotetrapods.[3] These diverse nanostructures are popular in almost every field substantially used in catalysis,[4] immunoassays,[5] drug delivery to cancer cells,[6] detection/ sensing strategies[7] and many other biomedical applications by measuring changes in LSPR, and surface-enhanced Raman scattering.[8]

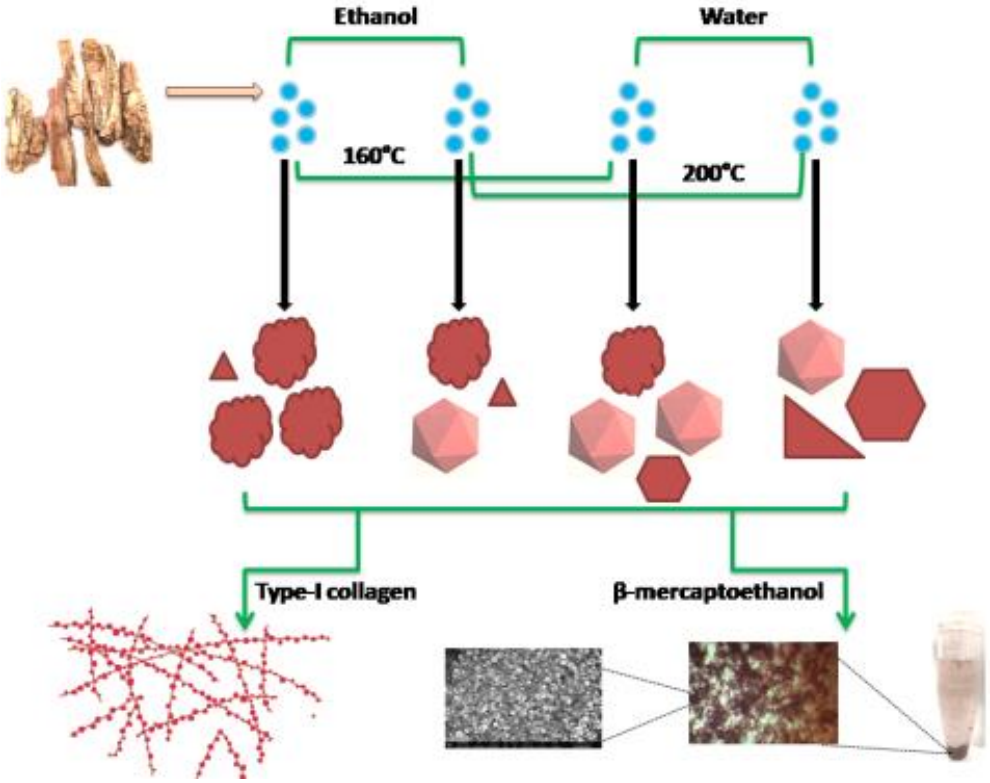

Figure 4.1: Schematic illustration of the effect of synthesis route for *Arjuna terminalia*-derived carbon quantum dots on the mechanistic formation of gold nanoparticles

The mechanistic control of carbon quantum dots on the growth and morphological inclination of gold nanoparticles has been studied in detail. Type-1 collagen increases the stability of the less-stable gold nanoparticles synthesized using water based carbon dots. Addition of β-mercaptoethanol into the salt-containing gold nanoparticle solution causes spontaneous "snowing" of the gold nanoparticles. The nanoparticles are highly biocompatible and the role of epoxy group on the carbon dot surface in the reduction and stabilisation of gold nanoparticles has been hypothesized.

4.1.2 Synthesis and Biological Applications of Gold Nanoparticles

In the recent years, significant research progress has been made using AuNPs for various biological applications like photothermal therapy, transfection, *in vivo* imaging, protein inhibition, DNA binding and calorimetric probing.[9, 10] For these

biological applications, AuNPs have to be carefully tailored laying special emphasis on the reducing and capping agents, the refractive index of the medium and the physical morphology of the AuNPs.[9]

Following the Turkevich–Frens classical-citrate method, many protocols were designed for chemical AuNP synthesis like the Brust–Schiffrin two-phase method, Weisner's nucleation growth method, Murphy and Han CTAB method and Perrault hydroqinone method to name a few.[1, 11, 12] Recently, the focus has shifted towards greener methods of AuNP synthesis to avoid synthetic toxic chemicals and other physical parameters. These methods are cost effective since they use biological mass like bacteria, fungi and plant extracts as reducing agents.[11] It has been reported that the biosynthesis of AuNPs involves weak interactions predominantly electrostatic forces, between the gold salt and the functional groups on the biomaterial attributed by alkaloids, flavonoids and terpenoids in plants in addition to many proteins and reducing carbohydrates in biota.[13]

4.1.3 Combining the Optical Properties of Both Gold Nanoparticles and CQDs

In 1718, Hans Heinrich Helcher noticed that boiled starch increases the stability of colloidal gold.[2] Recently, again carbon-based nanomaterials are gaining popularity because of the complex interplay of LSPR and photoluminescence physicochemical processes. Among carbon-based family, carbon quantum dots (CQDs) are gaining prominence as an advanced support material for the synthesis of AuNPs. They are nanometric carbon atomic clusters reported to act as both reducing and capping agents for AuNP synthesis in few minutes without the aid of any other chemical or physical agents. Compared to traditional environmentally benign reducers, CQDs lend a better control and uniformity to the reaction dynamics. Not only do

CQDs possess richly fluorescent and photoelectrochemical properties but also are excellent electron donors and electron acceptors making them ideal reducing or oxidizing agents. CQDs contain few hundred atoms of which only a fraction have free electrons lending them size-dependent properties. So their emission and absorption levels can be tuned according to their nanometric diameters. CQDs have a stronger reducing efficiency as compared to their natural precursors. Hydrothermal method is one of the simplest green approaches for synthesizing CQDs without adding any other physical or chemical agent.

CQDs have found a wide scope in biological applications because they are photoactive, biocompatible and easily identifiable *in vitro* or *in vivo* using confocal microscopy, flow cytometry and *in vivo* imaging.[14] They are physicochemically and photochemically stable and resist photobleaching. Combining the properties of AuNPs with quantum semiconductors opens a huge scope for unravelling the potential of such hybrid multifunctional materials. Therefore, it would be interesting to combine the optical and electrical properties of both AuNPs and CQDs to yield a robust material for biomedical and biosensing applications. The abundant peripheral oxygen-containing functional groups make CQDs hydrophilic helping them to act as a favorable scaffold whose surface charges help in the photoreduction and stabilization of the AuNPs in solution. Recently, there has been a surge in reports using CQDs for reducing and capping AuNPs.[15]

4.1.4 Use of *Arjuna terminalia* as the carbon precursor for the synthesis of CQDs and gold nanoparticles

Herein, we report the synthesis of gold nanoparticles using CQDs derived from the same source, bark of *Arjuna terminalia*, but subjected to different physical and

chemical conditions. The bark of *Arjuna terminalia* is known to possess medicinal attributes and is a green, inexpensive material. In this work, reductive CQDs were prepared via hydrothermal method in two solvents, namely water and ethanol, both subjected to two different temperatures, 160°C and 200°C. These four different CQD types were used as reducing and capping agents to synthesize AuNPs. The physical properties of nanosized gold are a strong function of its shape, size, inter-particle distance and protecting organic shell.[2] Through experimental analysis, this work reveals that the properties and reaction dynamics of these AuNPs are highly dependent on CQD characteristics. The stability of AuNPs can be strongly enhanced by collagen, an integral part of the extracellular matrix. It was also observed that β-mercaptoethanol forms a rapid and spontaneous supramolecular assembly with AuNPs. These robust biocompatible composite systems can be used in future as a dual-probe in bionanotechnology applications.

4.2 Results and Discussions

This report evaluates CQDs as the reducing and capping agent for the green synthesis and tailoring of AuNPs in detail. The aim is to engineer stable and biocompatible AuNPs for biomedical use utilizing carbon dots without the use of additional steps and toxic reagents. Four different greenish-blue fluorescent CQDs have been used to evaluate their effect on AuNP properties fabricated from the bark of *Arjuna terminalia* by hydrothermal carbonization.

4.2.1 Characterisation of the Four Variants of CQDs

To understand the effect of physicochemical factors on the intrinsic properties of CQDs, two parameters were explored- the reaction temperature of carbonisation and the solvent effect. CQDs were synthesized by the combination of different

solvents (ethanol, water) and hydrothermal temperatures (160°C and 200°C) to yield four variants denoted as E160, E200, W160 and W200. During the hydrothermal process, the high pressure of the system breaks the bonds of constituent biomolecules and metabolites of the plant leading to the formation of individual functionalised carbon nanocores which have great reducing potential and solubility in both solvents. After 8 hours of carbonisation and subsequent filtering through 0.22 µ membrane, all CQDs displayed different shades of brown in daylight. TEM images showed that all the CQDs were well dispersed and possessed quasispherical shape but their sizes were different as the average diameters lay in the range of 2-6 nm (Figure 4.2A). It was observed that the carbon dots synthesized at 160°C hydrothermal temperature were bigger than those synthesized at 200°C. Selected area electron diffraction (SAED) patterns determined the amorphous nature of the carbon dots indicated by the diffuse rings and absence of discrete uniform diffraction pattern as generally observed for crystalline materials (Figure 4.3).

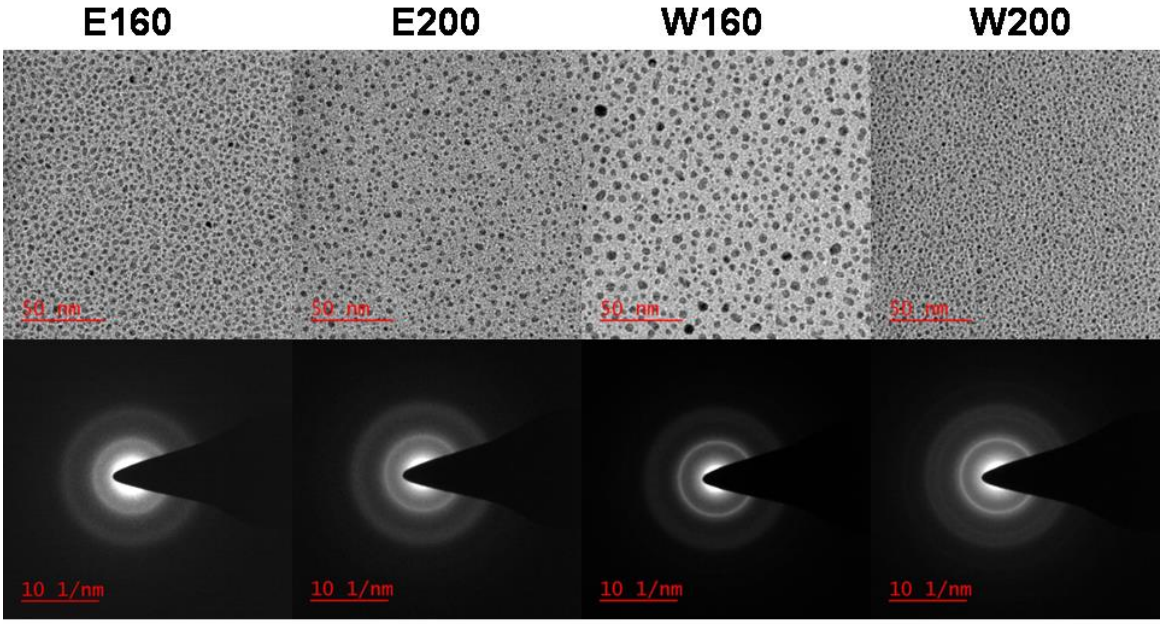

Figure 4.3: TEM images showing uniform distribution of CQDs (E160, E200, W160, W200), SAED patterns indicate amorphous nature

The UV-Vis absorption spectra (Figure 4.2B) of ethanol-based CQDs from 200-800 nm showed two peaks around 260 and 370 nm corresponding to the π-π* and n-π* transition from functionalised carbon like the −C=O− amide bond usually at 360 nm while the −NH− bond can promote the red shift of this band.[16, 17] For the water-based CQDs, a prominent peak around 280 nm observed. This also may be attributed to the π-π* or n-π* electronic transitions of carbon, nitrogen and oxygen double bonds. The absorbance spectra of both ECQDs and WCQDs show absorbance peak maxima in the 200-350 nm range that is typical of plant-derived CQDs emitting blue fluorescence.[18, 19] It is also to be noted that the solvent largely contributes to the absorbance peak shifts even though the starting material is the same. All carbon dots showed typical excitation-dependent photoluminescence spectra (Figure 4.4).

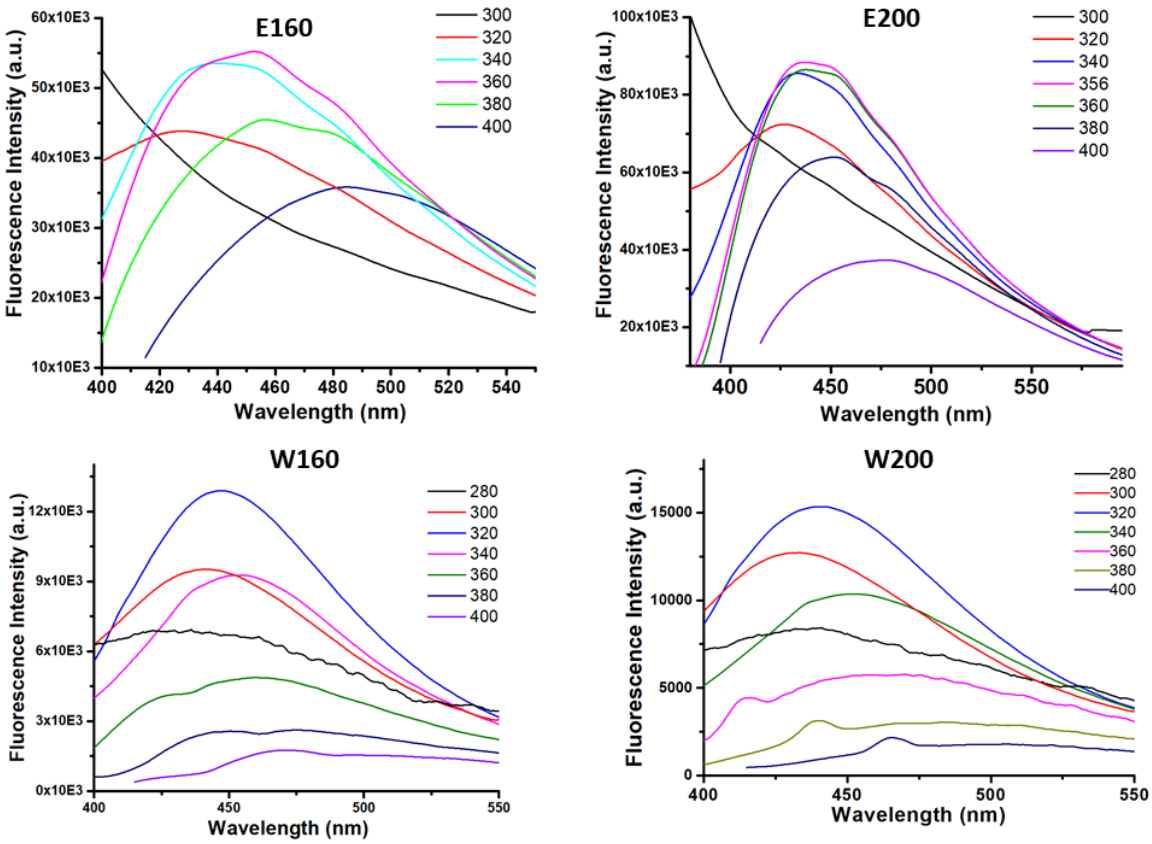

Figure 4.4: Excitation-dependent photoluminescence spectra of CQDs (E160, E200, W160, W200) ; excitation wavelength given in nm

Few reports describe the role of solvent effect in affecting PL properties.[20] E160 and E200 showed maximum emission at 450 nm when excited at 360 nm while W160 and W200 showed fluorescence emission maxima at 440 nm when excited at 320 nm. This demonstrates the difference in energy levels solely because of different solvents. The innate size of CQDs is another reason responsible for their varying PL properties. Hydrothermal temperature does not seem to cause a significant shift in the emission spectra. Nevertheless, as the carbonization temperature increases, the fluorescence intensity of the carbon dots also increases. The time-resolved fluorescence decay curves showed an average lifetime of 3 ns (2.914 ns for E200; 3.055 ns for W200) when fitted into a tri-exponential function (R^2=0.999) for all the CQDs hinting at similar energy exchanges and rapid radiative recombination caused due to similar functional groups and carbon core of CQDs (Figure 4.5). This is in tandem with most carbon dot fluorescence lifetimes reported.[19]

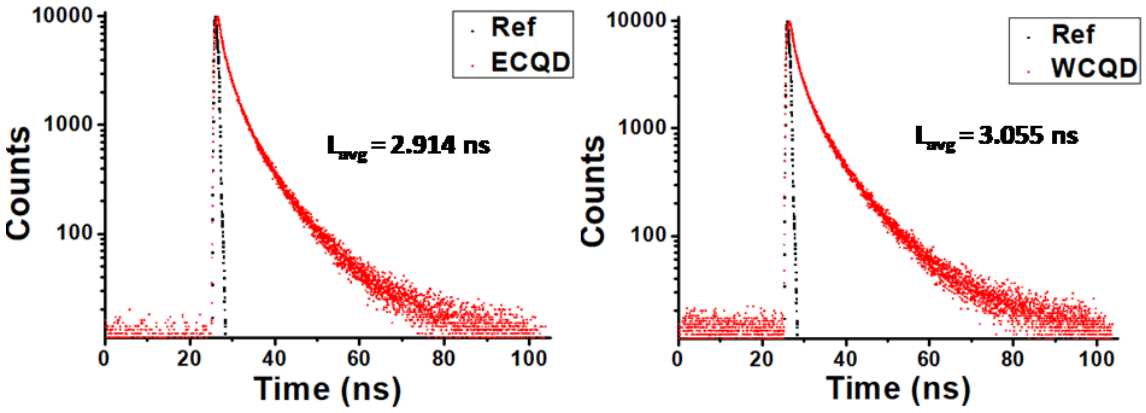

Figure 4.5: Fluorescence emission lifetime of CQDs (E200, W200)

Further, FTIR analysis revealed the structural information derived from the surface functional groups on CQDs (Figure 4.2C). The FTIR spectrum shows peak analogy within both ECQDs as well as within both WCQDs. The spectrum shows a

prominence of both sp^2 and sp^3 hybridized functional groups mainly comprising carbon conjugated with nitrogen and oxygen. A broad peak centred around 3423 cm^{-1} in ECQDs and 3415 cm^{-1} in WCQDs indicates phenolic stretch (OH) where ethanol itself contains OH group and partial stretch contributed by primary and secondary amines/amides (NH). Two additional small peaks in ECQDs at 2920 cm^{-1} and 2850 cm^{-1} are attributed to the alkyl stretches of the sp^2 and sp^3 hybridised carbon contributed by ethanol itself. It is an aliphatic alcohol having σ-bonds that contribute to the different vibrational energies in infrared region which appear as its signature peaks. The synthesized samples may also be rich in aldehyde content. Three consecutive peaks in ECQDs at 1723 cm^{-1}, 1613 cm^{-1} and 1448 cm^{-1} represent aldehyde/ ketonic/ carboxylic stretch (C=O), NH bend with alkene stretch (C=C) and alkyl ($–CH_3$) scissoring respectively. The last peaks at 1023 cm^{-1} in ECQDs and at 1078 cm^{-1} in WCQDs correspond to the C-O vibration stretch in ester/ ether. Peaks at 1621 cm^{-1} and 1409 cm^{-1} for WCQDs signify alkene stretch/ amine bend and alkyl bend respectively. Most of these oxygen and nitrogen rich functional groups provide polarity and hydrophilicity to each of the samples. Slight differences in peak positions indicate that the solvent plays an important role in the hydrothermally-effected surface passivation of the CQDs. This is an important factor to consider for initiating, maturing and stabilizing the growth of AuNPs.

Zeta potentials of each of the CQD forms were calculated to estimate the surface charge at the interfacial double layer. It was found that all the CQDs possessed a slight electronegative surface charge (W160: -10 eV, W200: -4.2, E160: -3.4 mV, E200: -1.5 mV) making them ideal reducing agents for AuNP synthesis.

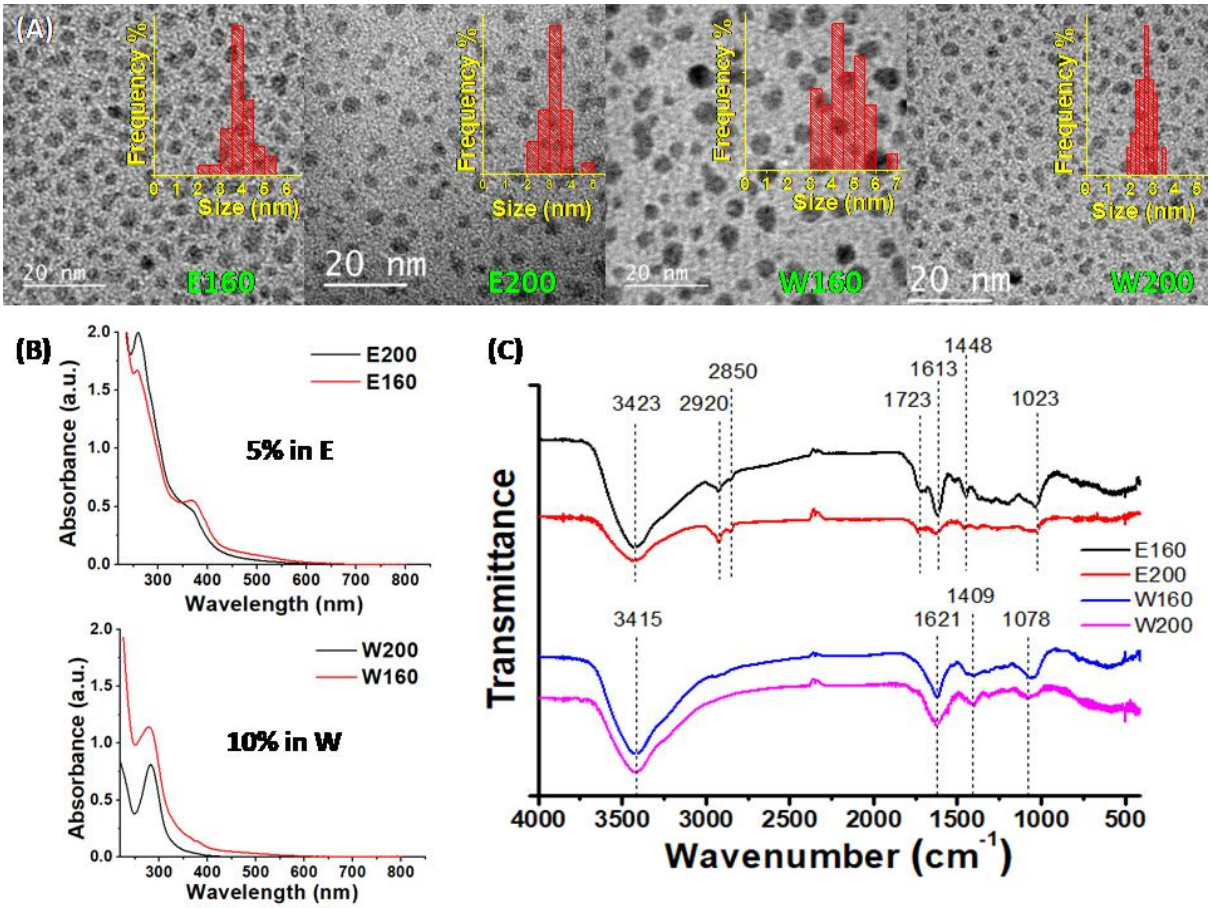

Figure 4.2: Characterization of CQDs (A) TEM images of CQDs (E160, E200, W160, W200) (B) UV- Vis absorption spectra of ECQDs and WCQDs (C) FTIR spectra of CQDs (E160, E200, W160, W200)

4.2.2 Synthesis and Growth of AuNPs

The nucleation and growth of AuNP discrete nanostructures is sensitive to the reducing and capping agent. It is hypothesized that parameters like different diameters, surface functionalisation and solvent environment of CQD may play a crucial role in shaping AuNPs. Conversely, the optical properties of CQDs directly get affected by the SPR frequency of the metal nanoparticles.[21] This may be caused by reverse electron transport from CQD to AuNP or charge tunnelling into the core affecting energy level transfer.[22] Therefore, the underlying physicochemical processes are very interesting to study because of the complicated interactions involved at the nanoscale.

Figure 4.6: CQD concentration- dependent Synthesis of Gold Nanoparticles. The four rows represent the use of E160, E200, W160 and W200 respectively showing most spontaneous reaction with E160 and least with W200 using CQD concentrations 0.025-0.5 v/v

The influence of different CQD synthesis conditions on the optimal catalysis of AuNPs has been explored (Figure 4.6). Many chemical reducing and capping agents like citrate, hydroquinone, tetraoctylammonium bromide (TOAB) with $NaBH_4$ and many more have been classically used to gain specific controls on the gold particle synthesis. It is not easy to control the size and stability of large nanoparticles. CQDs have the potential to be popular reducing and capping agents, both, by tuning their reaction conditions as they are easy to synthesize, non-cytotoxic and fluorescent at the same time. The cationic Au^{3+} ions from chloroauric acid get reduced to Au^0 by the negatively charged groups on the surface of CQDs acting as electron donors. These peripheral charges may also help in stabilizing AuNPs on the carbon functionalized

templates preventing aggregation. The formation of AuNPs was apparent visually as the colour of the solutions changed from almost colourless to pink shades ranging from rosy pink and magenta to purple (Figure 4.7A).

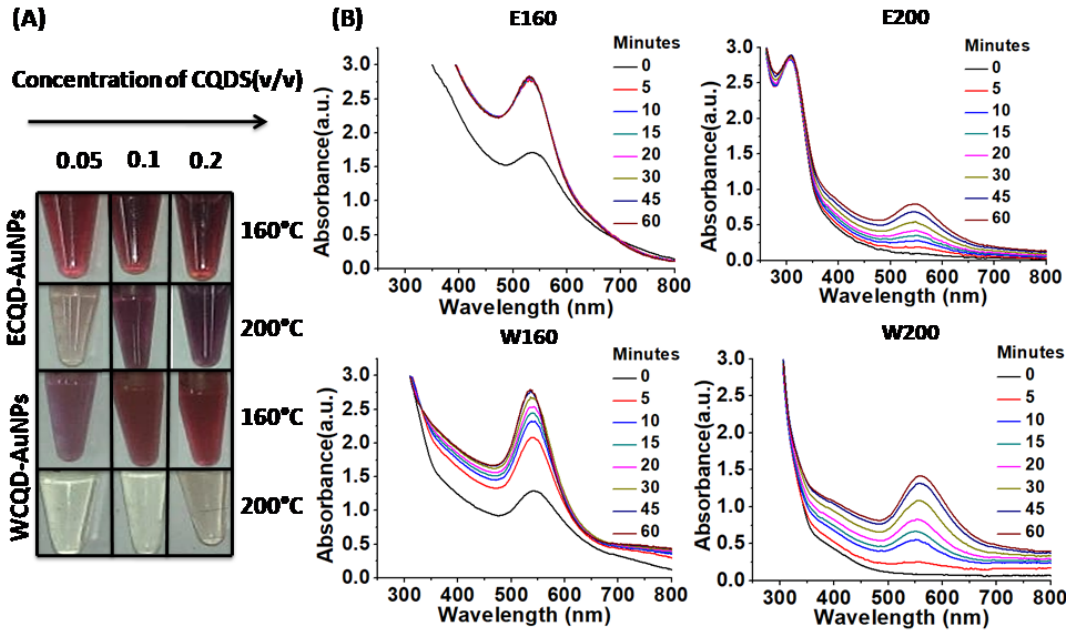

Figure 4.7: Synthesis of Gold nanoparticles (A) Colorimetric inspection of gold nanoparticle synthesis under different physicochemical conditions. $HAuCl_4$ concentration- 0.5 ml, 1.5 mM; CQD concentrations- 0.5 ml, 0.05/0.1/0.2 v/v in DI (B) UV-Vis absorption spectra of AuNPs synthesized by E160, E200, W160, W200; continuous readings taken for 1 hour from the start of reaction

E160 and W160 aided AuNPs showed lighter hues as their characteristic SPR absorption bands appeared at 530 nm and 535 nm[15] respectively. The other two AuNP samples (using E200, W200) appeared darker purplish pink in colour corresponding to their SPR absorption bands at 545 nm and 560 nm respectively (Figure 4.7B). The shape and number of atoms in AuNPs decides the position of the plasmon band. The interacting material, in this case CQDs, affects the LSPR width, intensity and position by its complex optical constant. Nanospheres or nanodecahedra find their plasmon peak centred at 550 nm.[21]

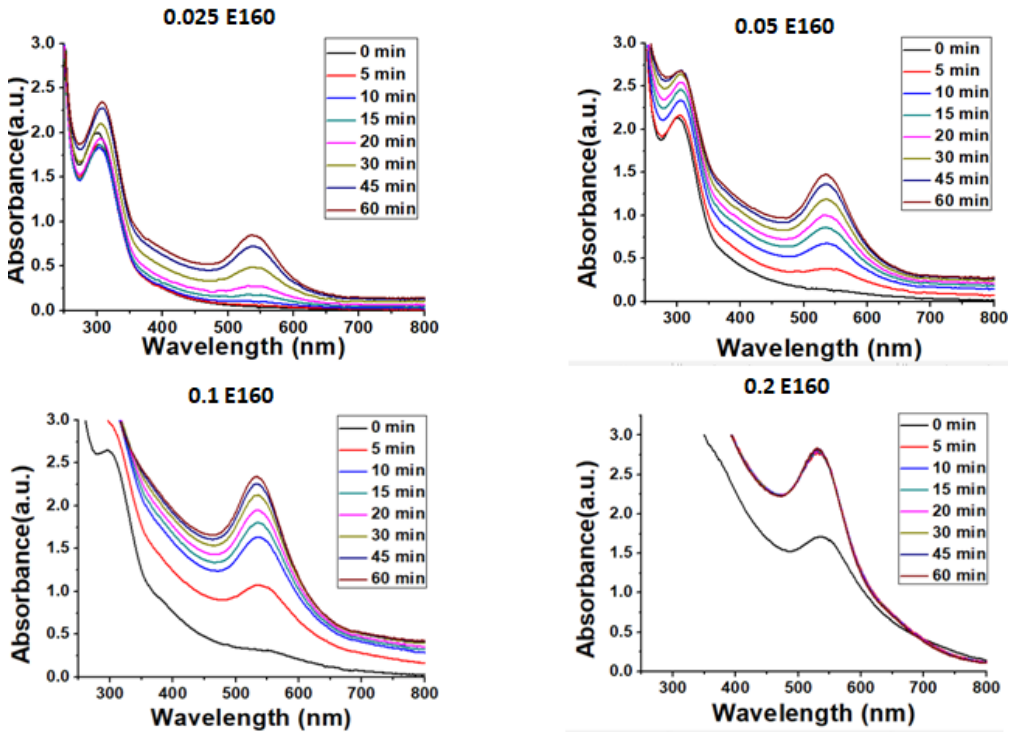

Figure 4.8: UV-Vis absorbance spectra of AuNP-ECQD160 showing time-dependent SPR peak from the start of AuNP synthesis reaction

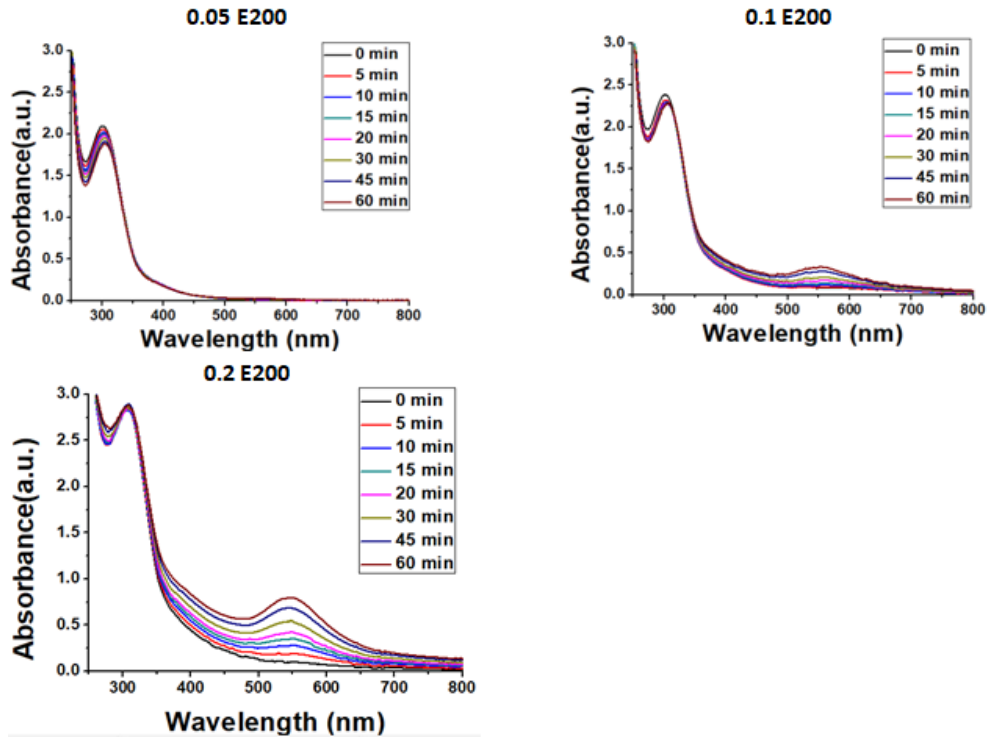

Figure 4.9: UV-Vis absorbance spectra of AuNP-ECQD200 showing time-dependent SPR peak from the start of AuNP synthesis reaction

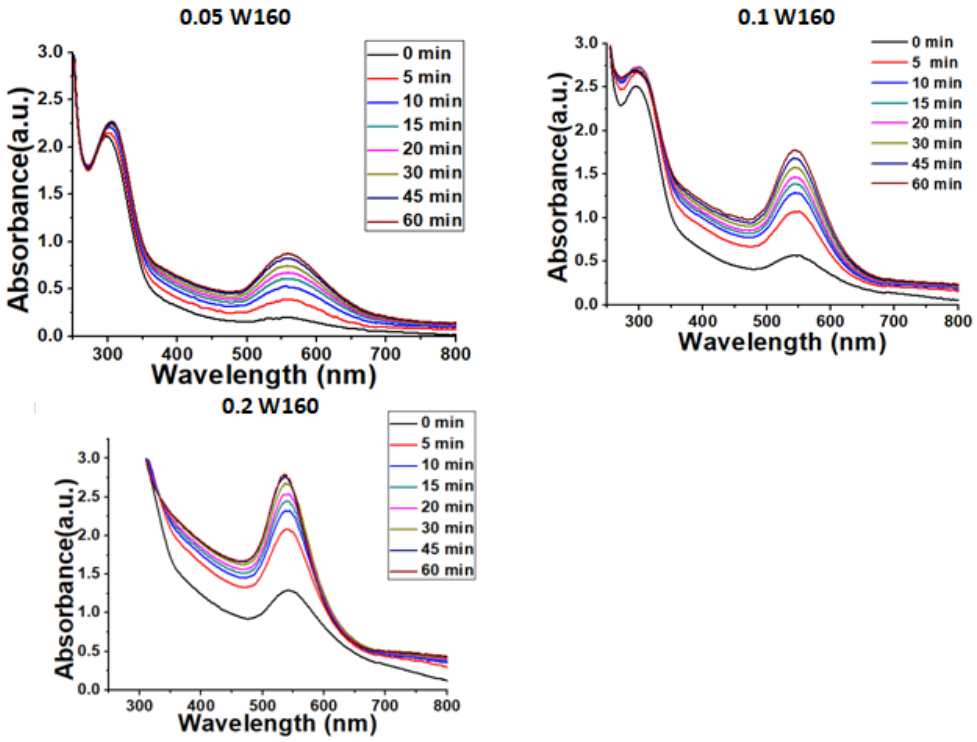

Figure 4.10: UV-Vis absorbance spectra of AuNP-WCQD160 showing time-dependent SPR peak from the start of AuNP synthesis reaction

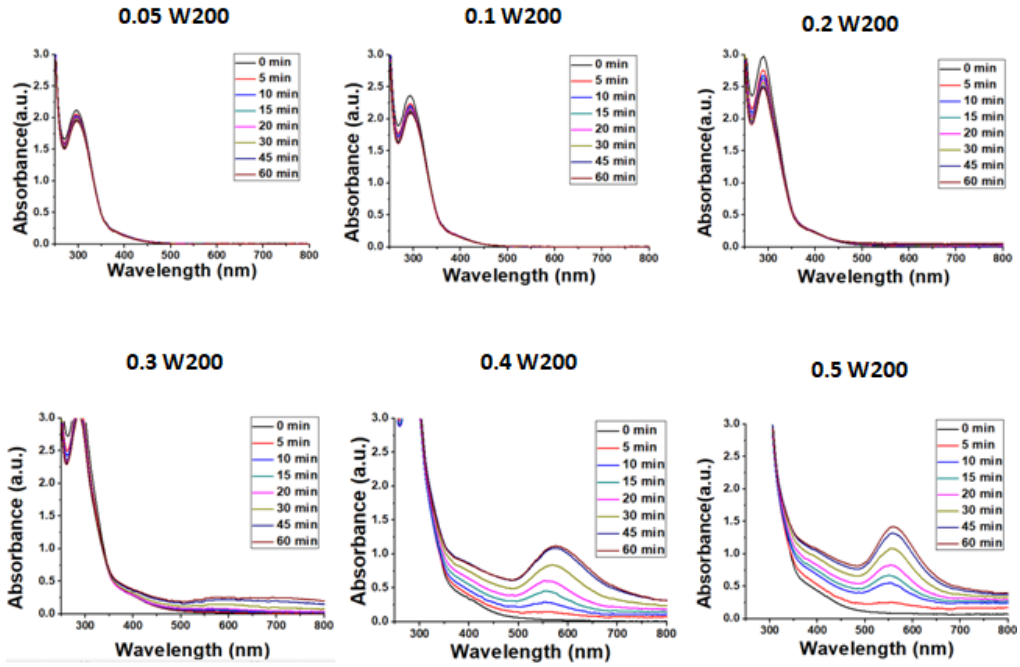

Figure 4.11: UV-Vis absorbance spectra of AuNP-WCQD200 showing time-dependent SPR peak from the start of AuNP synthesis reaction

The concentration of $HAuCl_4$ was kept constant (0.75 mM) while CQDs were used in different dilution multiples (Figure 4.8-4.11). It was observed that the concentration of CQDs was directly proportional to the absorption peak and inversely proportional to the reaction time. Three different volumes of each CQD solution were used for the reaction (0.05, 0.1, 0.2 v/v). A noticeable observation was that the AuNPs aided by CQDs carbonised at 160°C showed a very rapid reaction even with lower amounts of CQDs. The most spontaneous reaction took place using E160 which even yielded AuNPs on using very low volumes of E160 (30 µl /ml). With 0.2 v/v concentration, it reached LSPR peak maxima with incubation time of few seconds which was constant thereafter. On the other hand, W200 proved to be the least amenable reducing agent with slowest reaction time. Even at a concentration of 0.2 v/v, AuNPs took more than an hour to form but as the concentration of W200 was increased, the AuNPs formed more readily. This can easily be illustrated by the absorption spectra recorded for each of these conditions for a time period of one hour at 0.2 v/v CQD concentration (Figure 4.7B). It is evident that E160 yields AuNPs at the fastest rate followed by W160. This proves that the surface functional group composition of the 160°C carbonised CQDs have a better reducing potential than those carbonised at 200°C. E200-AuNPs show slow and steady peak increase while W200-AuNPs have a negligible peak even after an hour which increases after few more hours. It can also be concluded that ethanol-based CQDs facilitate faster AuNP reactions and higher SPR peaks as compared to water-based CQDs. It is also established that as the AuNP concentration increases, the absorption peaks of CQDs elevate minimally.

4.2.3 Morphology and Structural Elucidation of AuNPs

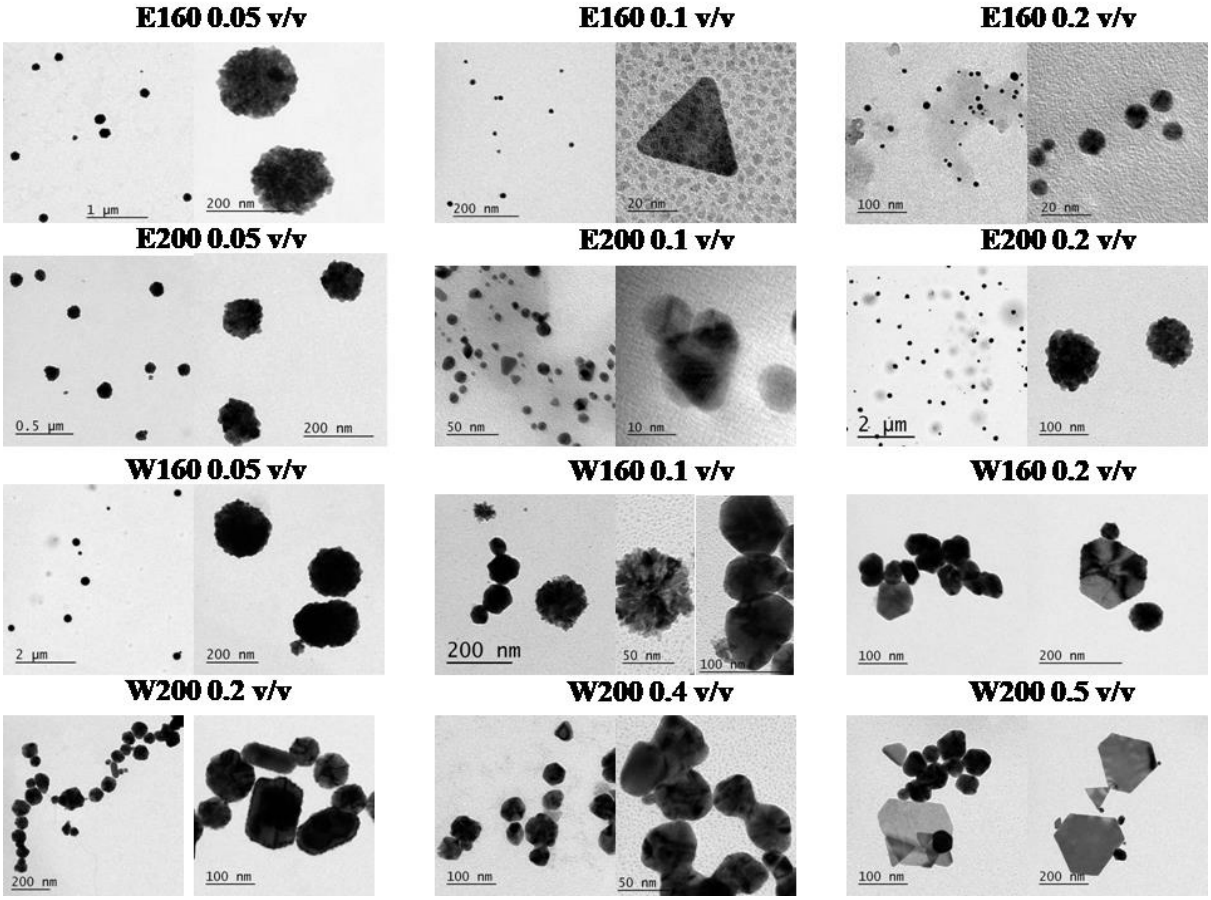

Fig 4.12: TEM images of AuNPs under different conditions. Morphology gradient of gold nanoparticles dependent on CQDs (concentrations- 0.05, 0.1, 0.2 v/v for E160, E200, W160, W200; solvent- ethanol/ water; CQD hydrothermal temperatures-160^{0}C and 200^0 C)

Transmission electron microscopy (TEM) was utilized to shed light on the morphological order and size distribution of AuNPs and to understand the structural direction and control lent by CQDs on the formation of AuNPs (Figure 4.12). It has often been reported in literature that the concentration of reducing biomass is interrelated to the morphology and size of AuNPs. Therefore it is believed that specific functional groups and their frequency on the surface of CQDs must be directly responsible for lending different shapes to AuNPs. The sum of all present functional groups on the CQD surface may decide their net reduction potential. The role of

hydroxyl groups has often been implicated in the reduction of metal precursor salts.[16] One notable hypothesis is that the interaction of gold atoms with aldehydes and ketones direct them towards flat triangular shape.[3] The final SPR peak depends on multiple factors like the size, shape and environment of AuNPs.[23]

For TEM characterisation, each solution was drop-casted onto carbon-coated copper grids. It was noted that the AuNPs appeared as dark discrete nanocrystals surrounded by lighter uniformly distributed CQDs (average size less than 6 nm) promoting reduction reaction and capping the nanostructures to prevent aggregation.

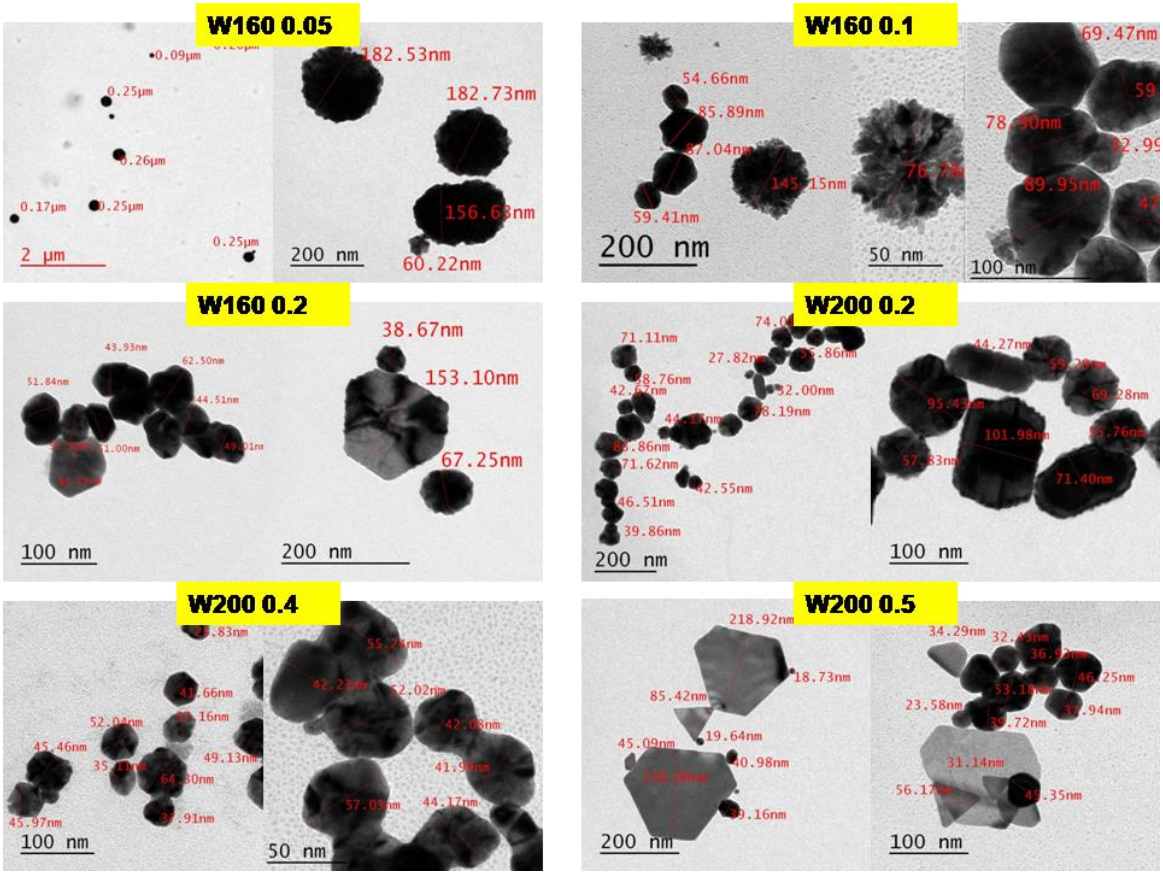

Figure 4.13: TEM diameters of WCQD-AuNP samples

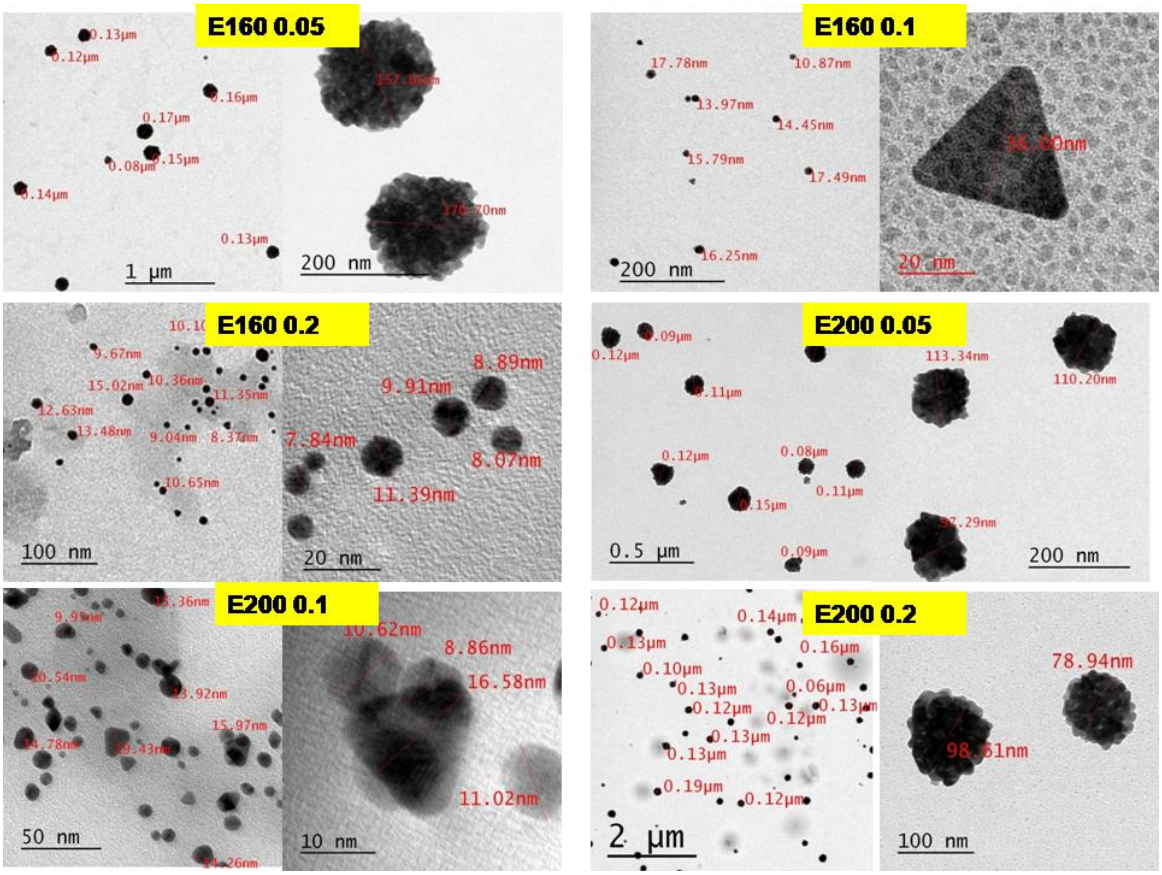

Figure 4.14: TEM diameters of ECQD-AuNP samples

All different CQD conditions had an effect on the final morphology of the AuNPs with respect to their morphology and diameters (Figure 4.13-4.14). It was observed that when less CQD was incorporated into the reaction (0.05 v/v), the AuNPs formed nanoflower morphology (Figure 4.15) dispersed in solution in E160, E200 and W160 AuNP samples. As the concentration of CQDs was increased, the AuNPs formed more defined multiply twinned phases, majorly resulting in icosahedral spheroids most pronounced in WCQD-based samples. Meanwhile E200 based AuNPs still possessed nanoflower and nanospherical shapes dispersed more evenly in solution. E160-AuNPs contained the most uniformly-dispersed singular and stable spheres. Mostly, truncated icosahedrons are formed after equilibrium shape is attained.[2] The average size of most solid polycrystalline nanoparticles and

nanoflowers ranged between 80-120 nm while small nanoparticles (~10 nm) served as building blocks of nanoflowers.

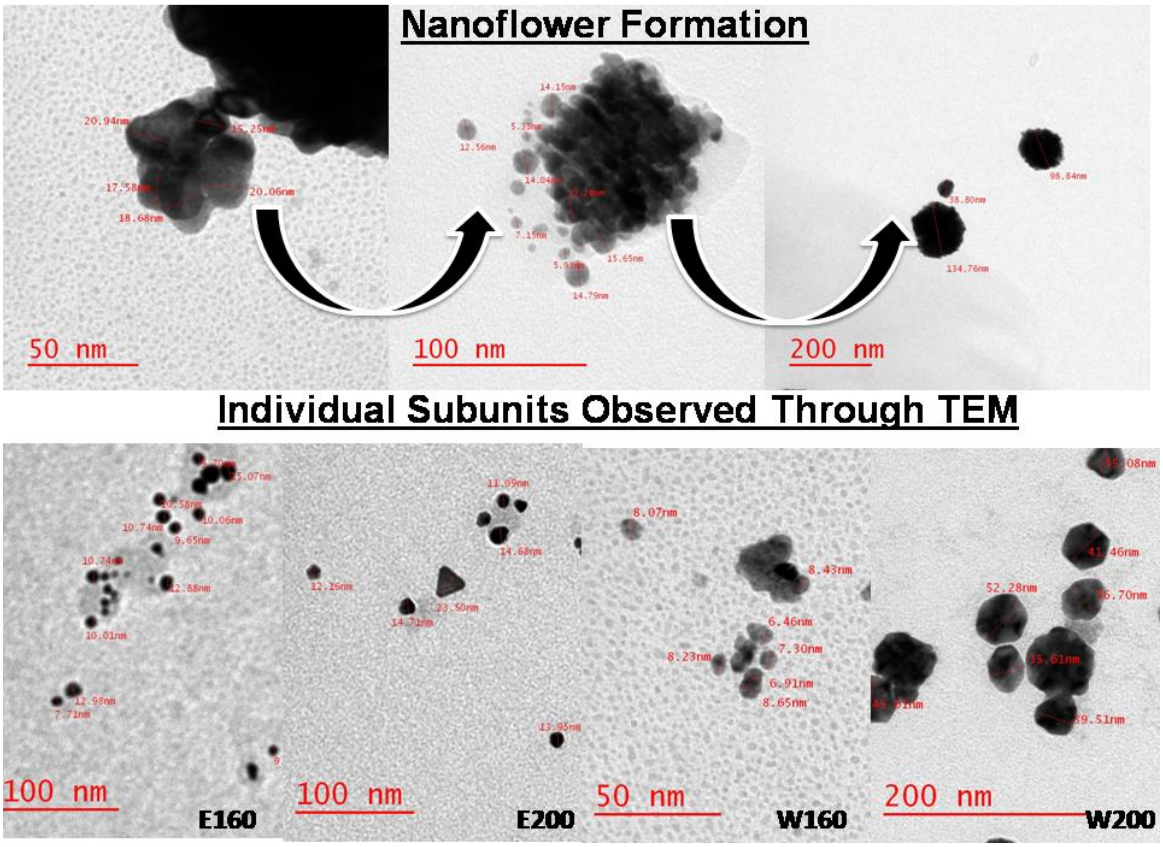

Figure 4.15: Formation of nanoflowers from small subunits of spherical AuNPs; individual smallest subunit TEM images of AuNP samples

In case of E160- and E200- supported AuNPs, spherical morphology is favoured with sparse flat triangles and they are more evenly dispersed than water-based AuNPs. E160-AuNPs contained more distinct small individual crystals that stayed non-aggregated showing stable dispersion as compared to E200-AuNPs which had more spherical aggregates (nanoflowers) made from smaller units. On the other hand, W160 (0.05 v/v) had very similar effect as E160 (0.05 v/v) creating nanoflowers. However, as the concentration was increased, more truncated spheroids with small average diameter of less than 20 nm were formed. W160 (0.1 v/v)

presented transitional morphologies with both nanoflowers and quasispherical icosahedrons leading to more chiselled closely spaced geometries in W160 (0.2 v/v). Lastly, as AuNP formation only began in W200 (0.2 v/v), three dilutions (0.2, 0.4, 0.5 v/v) were chosen for inspection. It was observed that W200 (0.2 v/v) aided AuNPs formed well-defined pentagonal/ hexagonal prisms and icosahedral shapes. On increasing the concentration to W200 (0.4 v/v), AuNPs fused into one another losing their well-defined edges to form branched morpholology. It is proposed to possess high localisation of surface plasmon modes which could be useful in SERS applications.[24] Further W200 increment (0.5 v/v) led to the prominent structuring of flat hexagonal plates and planar triangles in addition to multiple convex polyhedrons. Flat triangles seem to be formed by rapid reduction often accompanied by large near-infrared absorption. The fluid-like surface of flat geometries arises from the stresses leading to buckling of the extremely thin nanosheets.[3] The decahedral shape is recognized by five-twin boundaries of (111) crystal faces.[24] Lastly, it is worth mentioning that the halide ions also play an essential role in shaping AuNPs.[24] It was also observed here that platonic shape control is gained by adjusting concentration of CQDs.[25]

It has been reported that unusual nucleation and growth kinetics of AuNPs result in the presence of the antibiotic cephalexin.[26] Polycrystalline geometries are a result of twin planar defects causing anisotropic growth of AuNPs.[27] This results in a bathocromic shift in the absorbance spectra of AuNPs because of sharper vertices and fewer faces.[23] These results are in agreement to previous reports which have shown that as the amount of plant-derived extract is increased the ratio of spherical nanoparticles to planar triangular/ hexagonal shapes decreases.[23] Besides, the average size of the spherical particles also increases. Apart from twin-planar defects in face-

centred cubic (FCC) metals usually having hexagonal close-packed system, where multiple twinning leads to icosahedral and decahedral shapes, another kind of defects called stacking faults lead to hexagonal and triangular plates.[28]

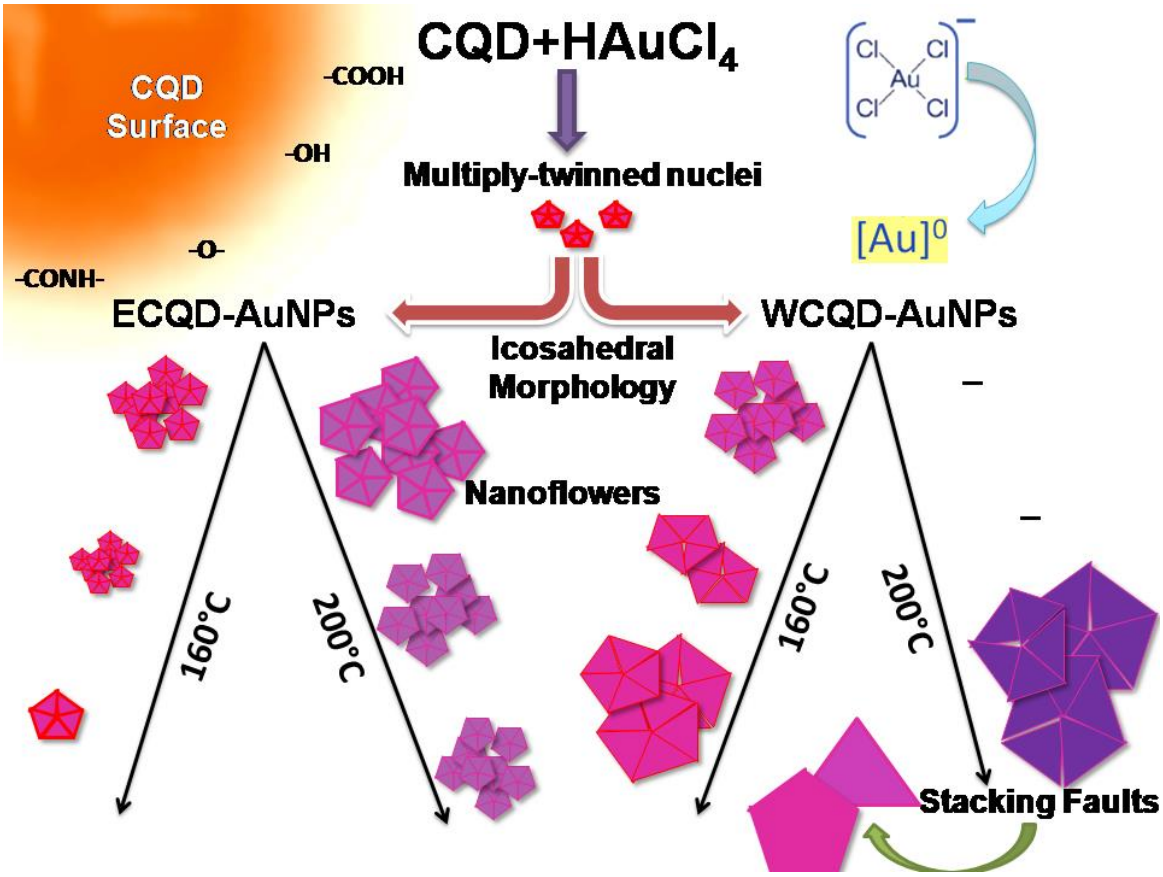

Figure 4.16: Schematic mechanism for detailed explanation of the synthesis and growth of AuNPs regulated by CQDs

4.2.4 Detailed Characterisation of AuNPs

For further phase and structural analysis of the nanoparticles, HRTEM and selected area electron-diffraction (SAED) patterning was studied. Figure 4.17A shows the HRTEM image of E160-AuNPs and SAED pattern for crystalline flat triangles in W200-AuNPs. The HRTEM images revealed the nanocrystal lattice fringes having an interplanar spacing of about 0.2 nm. They were assigned to the most commonly found (111) planes of face-centered cubic (FCC) gold. The selected area electron diffraction

(SAED) rings revealed the poly-crystalline organization of the AuNPs. All four AuNP samples reduced by 0.2 v/v CQDs displayed diffraction rings corresponding to the (111), (200), (220) and (311) signature gold FCC planes.[23] Hexagonal arrangement of the diffraction spots denotes (111) arranged planes that grow anisotropically to merge at the twin plane defect boundaries.[23] They eventually form polyhedrons, planar triangles and hexagons.[23] The XRD plotted data well supports the SAED information as the sharp peaks denote strong Bragg reflections at 38.1, 44.5, 64.5 and 77.7 2θ values indicating (111), (200), (220) and (311) crystal lattice of FCC gold respectively (Figure 4.18). (111) facets are the most common and thermodynamically favored planes for an FCC metal.[17, 21] It has been found that the kinetic control and selective surface passivation of AuNPs depends on metal complex reduction potential, metal ion availability and adsorbate binding strength.[28]

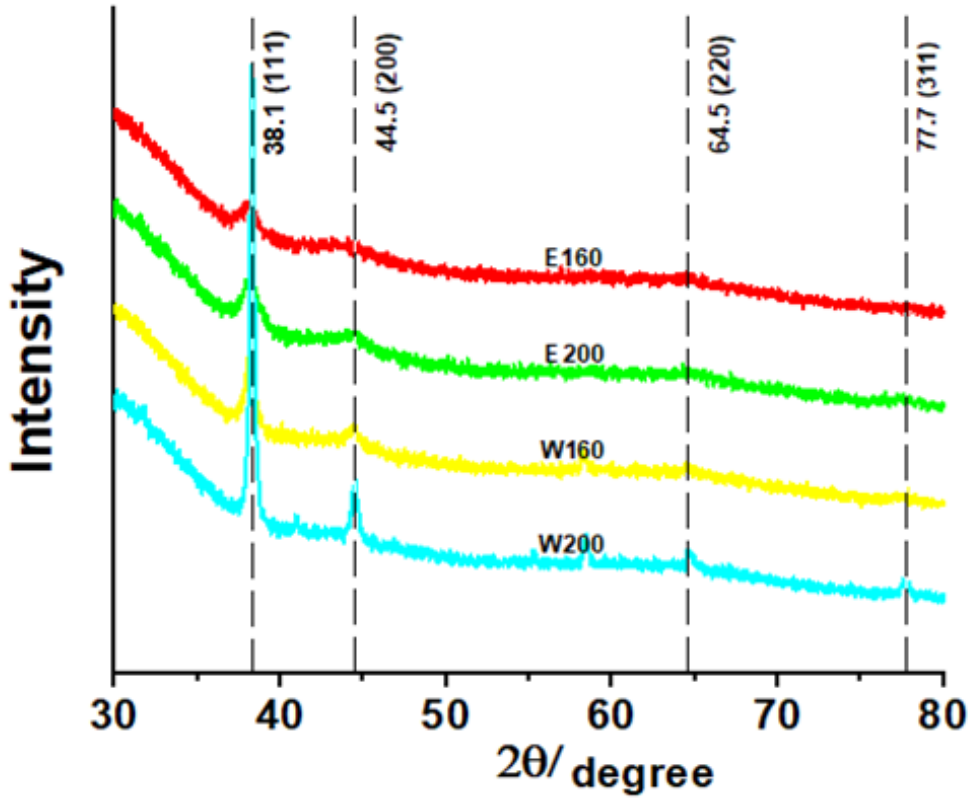

Figure 4.18: XRD pattern of AuNPs showing sharp crystalline Bragg's peaks at 38.1, 44.5, 64.5 and 77.7 2θ values

Photoluminescence spectra were recorded to understand the effect of AuNPs on the CQDs (Figure 4.17B) which relies on the AuNP size, the interparticle distance, the orientation of the dipole to the interparticle axis and the overlap of the CQD emission with the absorption of AuNPs.[2] In this study, the fluorescence of CQDs was found to be relatively quenched. The emission of the CQD-AuNP solution was recorded at 320 nm excitation wavelength for water based samples and 360 nm for ethanol based solutions. Fluorescence emission from a semiconductor quantum dot is strongly influenced by the nearby presence of AuNPs.[21] This property of fluorescence emission level modification is commonly utilized for sensing and detection applications.[22] The emission of 200CQDs is more than 160CQDs but the reducing ability is the opposite in both cases. Therefore, to make a dual signal probe, one would have to choose and optimise a trade-off condition which has the best emission/reduction ratio.

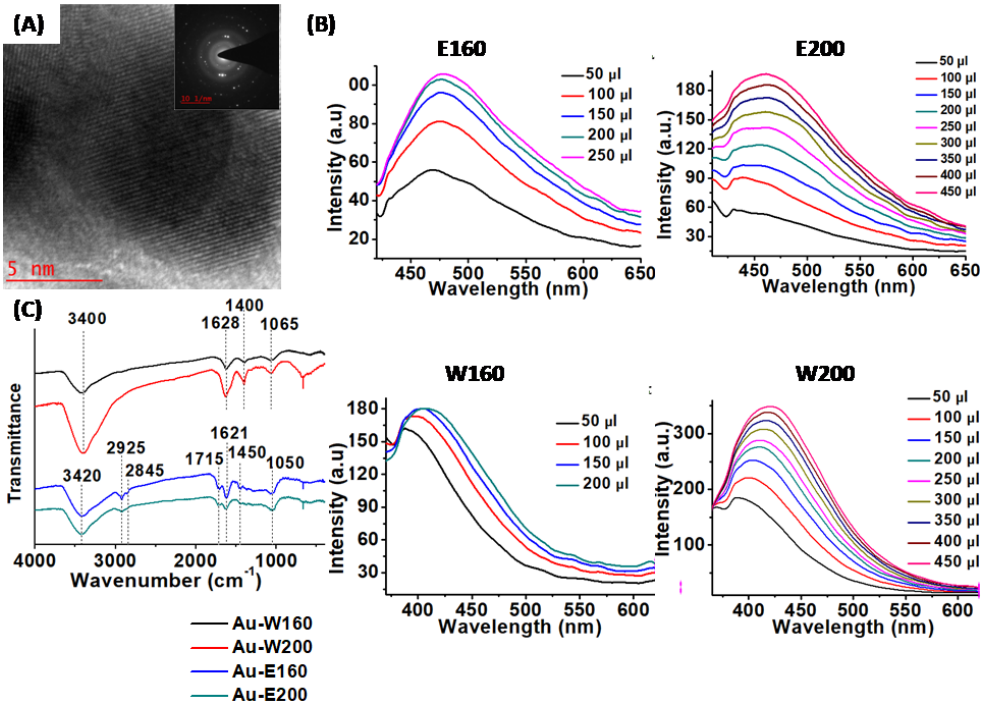

Figure 4.17: Characterization of AuNPs (A) HRTEM image (E160-AuNP) showing multiply-twinned AuNP surface boundary; SAED pattern for triangular plates in W200-AuNP (inset) (B) Concentration dependent photoluminescence curves of AuNP/ CQD solutions at 0.2 v/v concentration (C) FTIR spectra of AuNPs synthesized by CQDs (E160, E200, W160, W200)

The key factors thought to be responsible for affecting emission can be described in two divisions. The plasmonic field of the nanometal may either increase the excitation-decay rate of the CQDs causing fluorescence enhancement; or the dipole energy surrounding the AuNPs may disturb the radiative/ non-radiative decay fraction and reduce the quantum yield of CQDs, resulting in the quenching of fluorescence emission.[23] It is believed that defect-related emission originating from the CQD core is dominant over the surface emission by direct recombination. When the surface plasmons interact with CQD surface, direct electron transfers affect the normal emission of CQDs leading to quenching.[22]

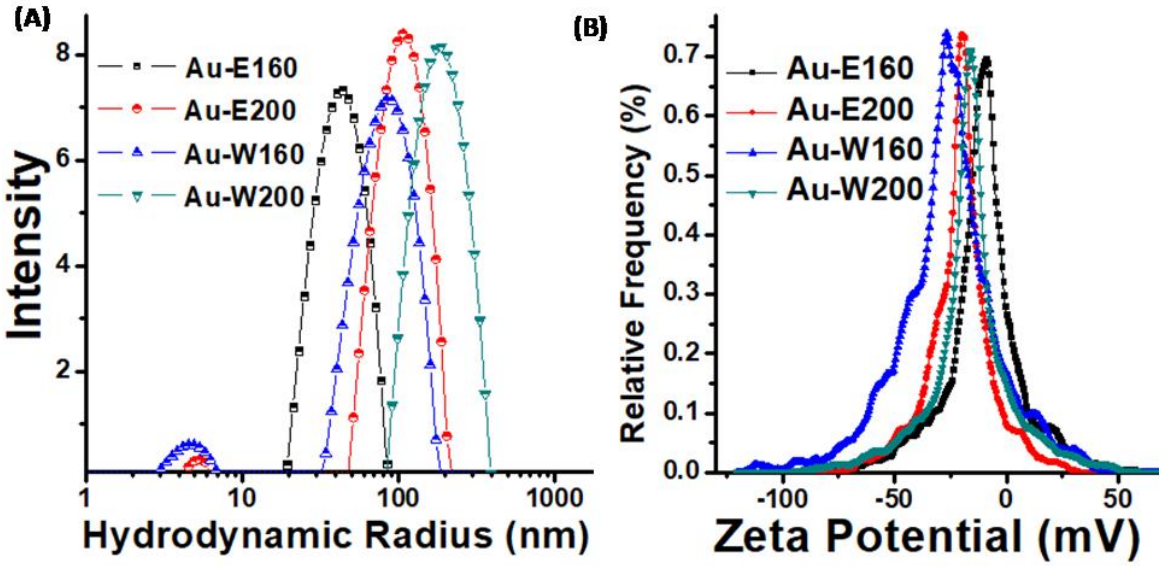

Figure 4.19: A) Hydrodynamic radii and B) zeta potential values of AuNP samples

The hydrodynamic diameter and count rate were gauged to determine the size distribution of all AuNP samples (Table 4.1, Figure 4.19). It was seen that the hydrodynamic diameter of E160-AuNPs was smallest (32 nm) while that of W200-AuNPs (189 nm) was maximum with small peaks around 5-6 nm representing the carbon dots or new gold nucleation sites. The AuNPs synthesized using 160-CQDs strikingly had a smaller diameter than those made using 200-CQDs. The AuNP solution had more than one-sized geometries having polydispersity index in the non-homogenous solution varying from 0.17-0.28. The inhomogeneity arises because the CQDs lead to fast reduction of AuNPs which not only gives rise to larger particles but also smaller particles due to secondary nucleation sites with miniscule dimensions. To avoid this, one can use seed-mediated growth or pH change to reduce reducing potential.[28] This data correlates well with the TEM analysis which showed nanoparticles within the same size range as measured using DLS. To separate out similar dimensional nanoparticle species, one can employ dialysis or repeated centrifugation according to a particular application using the same ratio of CQD

solution: solvent as dialysate. Unfortunately, current procedures still result in low yields of similar-dimensional particles requiring a purification step in order to eliminate out isotropic structures.[24]

To understand the role of physical electrostatic interactions stabilising the CQD-AuNP system, the zeta potential of the gold nanoparticles was assessed (Table 4.1, Figure 4.19). It was observed that the zeta potential at the interfacial double layer lay within the range from -10mV to -27 mV. This can be explained by the presence of cumulative net negative bilayer of CQDs capping AuNPs at the interface interspersed with chloride ions.

Table 4.1: Comparison between all 0.2 v/v CQD (E160, E200, W160, W200) assisted AuNPs for different parameters (Surface Plasmon Band (SPB), Average TEM diameter, DLS size, zeta potential and polydispersity indices.

AuNP Sample (CQD 0.2 v/v)	SPB (nm)	Average TEM Size (nm)	DLS Size (nm)	Zeta Potential	Polydispersity Index
E160-AuNPs	530	11	32	-10 mV	28.29%
E200-AuNPs	545	11 (Subunits) 120(nanoflower)	104	-20 mV	17.44%
W160- AuNPs	535	60	76	-27 mV	24%
W200-AuNPs	560	80	189	-16 mV	22.9%

When AuNPs were generated by using CQDs as the reducing agent, FTIR analysis was conducted again to shed some light on the functional groups participating in the reaction (Fig. 4C). The FTIR spectrum shows minor deviation from the previous spectrum of CQDs only. The H-bound hydroxyl peaks at 3400 cm^{-1} (Au-WCQDs) and 3420 cm^{-1} (Au-ECQDs) did not change significantly from their previous peak positions. Peaks of Au-ECQDs at 2925 cm^{-1} and 2845 cm^{-1} also did not vary much. Again all peaks within 1750-1400 cm^{-1} showed slight shift. The only peak showing considerable change is centred around 1050 cm^{-1} and 1065 cm^{-1} signifying the plausible role of C-O stretch. This functional group is present in epoxy, ethers, esters,

carboxylic acids and anhydrides. Therefore, the classic alcohol oxidation series is thought to play a role in the reduction reaction. Reports have hypothesized the role of aldehydes/ ketones (C=O) [3] and OH group[16] as the reducing groups.

CQDs reduce Au^{3+} in chloroacetic acid into Au^{0} which assembles into a multiply-twinned nucleation centre for bigger AuNPs after which CQDs stabilise AuNPs during the latter controlled growth phase where metal ion availability depletes. Increasing the concentration of CQDs increases the reductive potential and enables faster reactions directed by the active surface of functional groups present on the surface of CQDs. Ethanol-based CQDs seem to act as better reducing agents as they favour better yield and faster reaction kinetics.

In the present work, the dominant morphology was icosahedrons which were structured by stable and thermodynamically favoured 111 planes. These planes find energetically more favourable tendency to be built leading to multiple crystal domains or or "multiply-twinned nanoparticles. CQDs can be used for controlled growth rate and shape regulation of gold nanocrystals. The interplay of different conditions favour growth in different crystallographic directions for symmetrical 2D or 3D morphology. 160ECQD-AuNPs show geometrically reminiscent morphologies resembling that of a stable sphere hinting at their high stability in solution.

In addition to twin defects in FCC structure, stacking faults dominate on increasing W200CQD concentration where energy barrier is very low for the formation of planar triangles and hexagons. The negative surface charge on AuNPs shows the stabilising action of CQDs. However, AuNP synthesis is notoriously sensitive to different reaction kinetics offered by the conditions CQDs were

synthesized in. Understanding these differences in more detail can help in rationally optimising the synthesis conditions.

4.2.5 Computational Analysis of CQD-Gold Nanoparticle Interaction

In order to understand the interaction between AuNPs and CQDs as per this study, a 5x5 single layer of benzene rings was modelled for CQD. To it, functional groups were added as per the findings from FTIR studies. The geometry of CQD was fully optimized using the M06-2X/6-311G(d,p) level of Density Functional Level using Gaussian 16. AuNPs were modelled by taking an eight-atom cluster[29] and optimized using the LANL2DZ[30]. The complex was further optimized also at the M06-2X level by employing the 6-311(d,p) basis set for lighter atoms like C, H and O and by using LANL2DZ for gold atoms. The interaction energy is calculated between the optimized model of the complex with respect to free CQD and gold cluster. It is found that the complex is lowered in energy by 24.65 kcal/mol with the gold cluster being in proximity of the -O- atom from an epoxy group (Figure 4.20) which might hint towards the improvement in delocalization of electronic charge around the CQD in the presence of the AuNP.

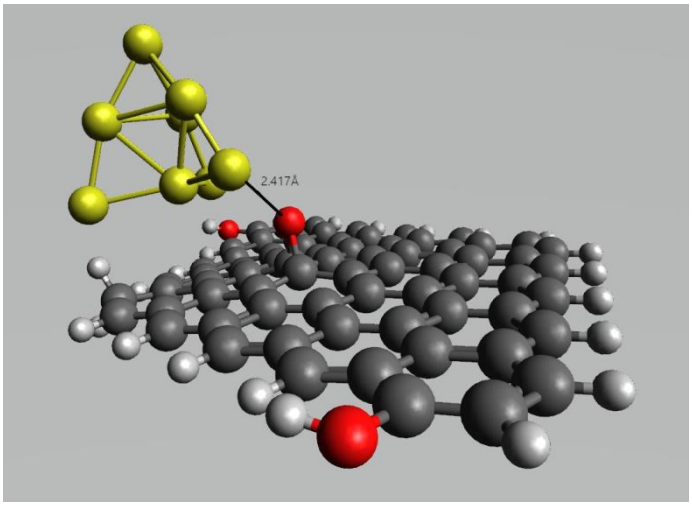

Figure 4.20: The most stable AU-CQD structure with the bond length (angstrom) is demonstrated having an -O- group

4.2.6 Cell Viability of MG-63 cell line in the presence of CQD-AuNP Solution

Biocompatability of AuNPs depends on their shape, size, concentration, net charge and surface functional groups.[31] Reports have shown that spherical AuNPs display the best biocompatibility.[28] Due to the large size of AuNPs, they enter cells by passive uptake through the endocytic pathway resulting in endosomal localization.[4] Maximum accumulation of AuNPs has been shown to occur in liver cells followed by the spleen. In this report, the cytotoxicity of AuNP-CQD solution was investigated by the standard MTT assay (Figure 4.21). All four AuNPs synthesized using 0.2 v/v CQDs, showed excellent biocompatibility with cell viability >98% as shown in figure inspite of difference in AuNP morphology, size and concentration.

AuNPs have been used for cancer cell targeting as they make cells more radiation sensitive. Their retention is affected by surface charge. Negatively charged AuNPs have larger retention time depending on interaction with stabilising proteins and same charge on lipid membranes. Passive uptake relies on EPR (permeability and retention effect) using extravasions of vectors through leaky blood vessels.[10] It has

been observed that maximum AuNP uptake is seen with particles having a diameter of 20-60 nm[32] but cytotoxicity is minimal for AuNPs <5 nm and >60 nm. Therefore it is a trade-off to choose the particle size carefully. Large cytotoxicity enhances bystander effect, where closeby cells get affected by reactive species generated by secondary electrons after radiation.[10]

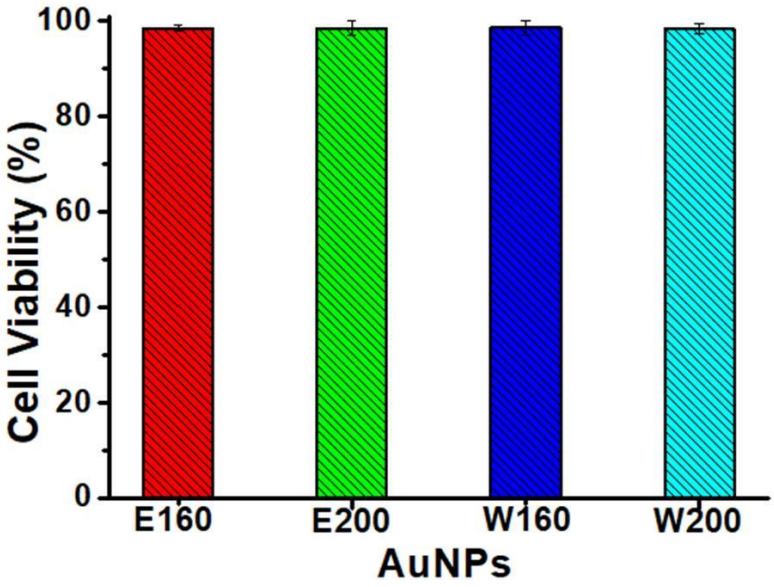

Figure 4.21: MTT Assay showing high biocompatibility of AuNPs

4.2.7 Stability of AuNPs Enhanced by Type-I Collagen

The synthesized AuNP solutions could stably be stored under ambient conditions for a variable period of time. The recorded stability of each solution varied from one another and the solution was considered stable till there was no visible aggregation and settling of AuNPs to the bottom of the microfuge tube. On losing stability, the AuNP solutions gradually fade in colour from pink to colourless as they noticeably aggregate to form the bulk arrangement. All samples with 0.2 v/v CQDs were checked for comparing stability. The E160- and E200- AuNPs were highly stable for more than one month. E160- AuNP was the most stable solution and it showed no

change even after 6 months. The W160 and W200 based AuNPs showed a gradual decline in stability W-200 being the least stable. It can be noted that both 160-AuNPs were more stable than their 200-AuNP counterparts. Moreover, ethanol-based AuNPs showed greater stability than aqueous CQD based AuNPs. However, for routine biomedical and drug delivery procedures, aqueous CQD-based AuNPs would be the suitable preference to enhance biocompatibility. It may be seen here that the long term stability and storage of AuNPs are contributed by multiple factors like the surface functional group composition stabilising them, the solvent and the hydrothermal temperature used to synthesize CQDs. The observed zeta potential (-10 to -27 mV) shows that all AuNPs have a tendency to stably exist in solution for a short period but over time, attractive forces between gold nanoparticles exceed over the repulsive forces leading to flocculation which depend on the afore-mentioned factors. Moreover, the aggregation tendency of AuNPs may partially control lifetime and *in vivo* uptake dynamics. The capping agent largely contributes to the passive uptake and half-life of the AuNPs in cells.

In order to improve the stability of WCQD-AuNPs, Type-I collagen from calf-skin was added into both the 0.2 v/v solutions (Figure 4.22). Three concentrations (0.025 %, 0.005 %, 0.0075 %, 0.01 %) of collagen and controls were kept at room temperature for one week (Figure 4.22C). Uv-Vis absorbance spectroscopy revealed that collagen considerably increased the stability of WCQD-AuNPs (Figure 4.22A&B). Optical microscopy images resolved the steady interaction of AuNPs on collagen fibres (Figure 4.22D). Since collagen serves to be a major component of the extracellular matrices, scaffolds and attachment supports for various tissues, it can serve as a biocompatible substrate for *in vivo* applications. It proves to be a perfect stabiliser for AuNPs suspended in aqueous WCQD mixtures.[33]

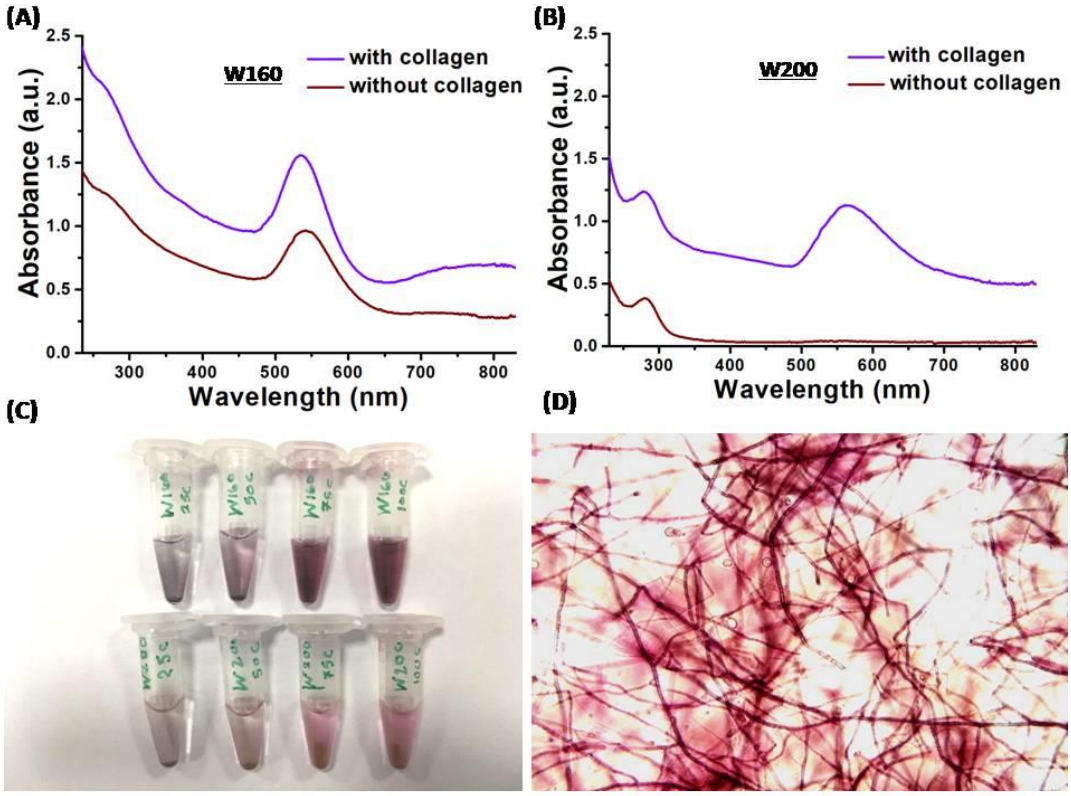

Figure 4.22: Role of Collagen as stabilizer for WCQDs (A-B) UV-Vis absorbance of WCQDs stabilized by collagen after 1 week (C) Visual inspection of AuNPs stabilized by 0.025%, 0.005%, 0.0075%, 0.01% collagen (Upper row-W160-AuNPs; Lower Row-W200-AuNPs) (D) Optical microscopy image of W160-AuNPs stabilized by collagen fibres

4.2.8 Role of β-mercaptoethanol in AuNP dispersion

Many researchers have used the high affinity between thiol-Au nanostructures to lend them some functionality.[1, 34] Thiolated derivatives have been used as bi-functional linkers to bridge AuNPs and DNA, peptides, PEG or other drug molecules.[35, 36] In the current report, β-mercaptoethanol was used to bind with the AuNP surface via its thiol-end by forming a dative bond and leaving a free hydroxyl group on the other end. Strangely, the solution appeared to form rapid visible aggregates growing in size in high ionic strength (5 mM NaCl) (Figure 4.23). These aggregates spontaneously formed nanonetworks and started sedimenting to the base of the centrifuge tube on account of their weight very similar to "snowing" (Figure 4.24).

This phenomenon observed by the naked eye indicates self-assembly of small molecules to combine into a supramolecular structure resulting from salt-induced phase segregation.[37] This superstructure undergoes surface plasmon coupling to finally yield bulk planes.[21] The solution showed a shorter peak with a bathochromic shift of absorption maximum corresponding to the size increment of AuNP complex by 20 nm. On adding β-mercaptoethanol to $HAuCl_4$ solution as control, to negate the contribution of CQDs, also showed similar nanoprecipitation subsequently settling down.

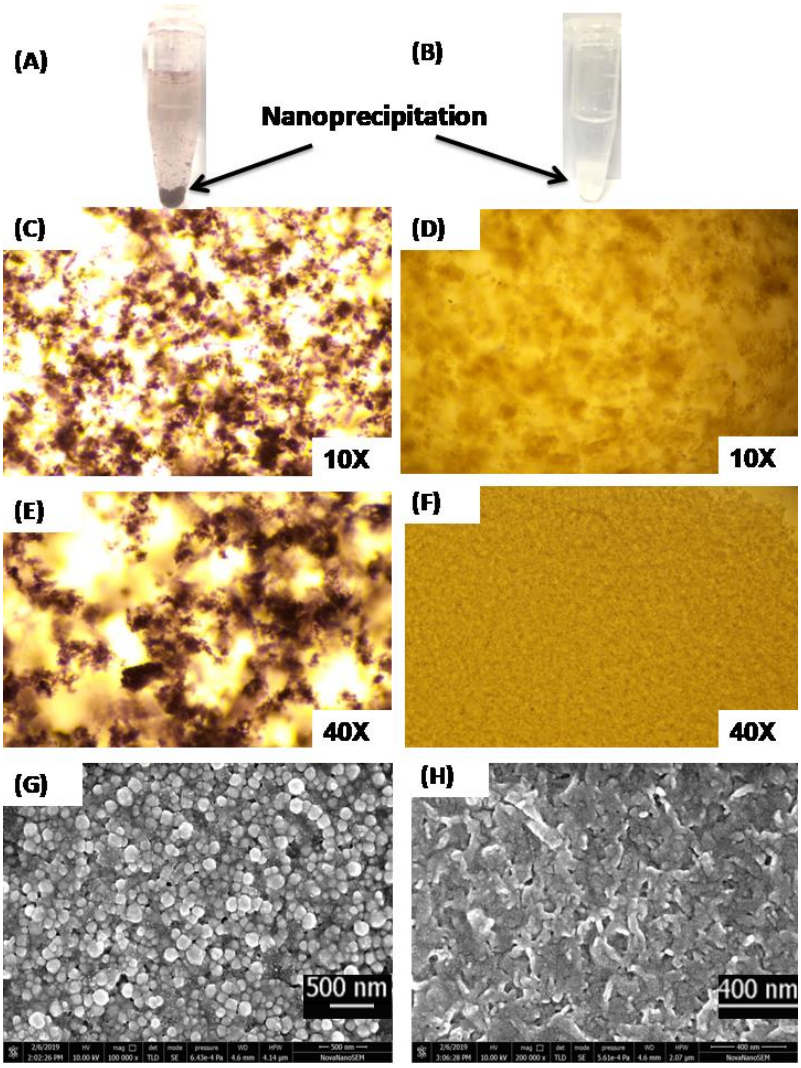

Figure 4.23: Snowing by β-Mercaptoethanol. Visual inspection of nanoprecipitation caused by 20 µl β-Mercaptoethanol in (A) W160-AuNPs (B) $HAuCl_4$. Optical microscopy images at 10x resolution (C) AuNP-snow (D) $HAuCl_4$-snow. Optical microscopy images at 40x resolution (E) AuNP-snow (F) $HAuCl_4$-snow. SEM imaging (G) AuNP-snow (H) $HAuCl_4$-snow

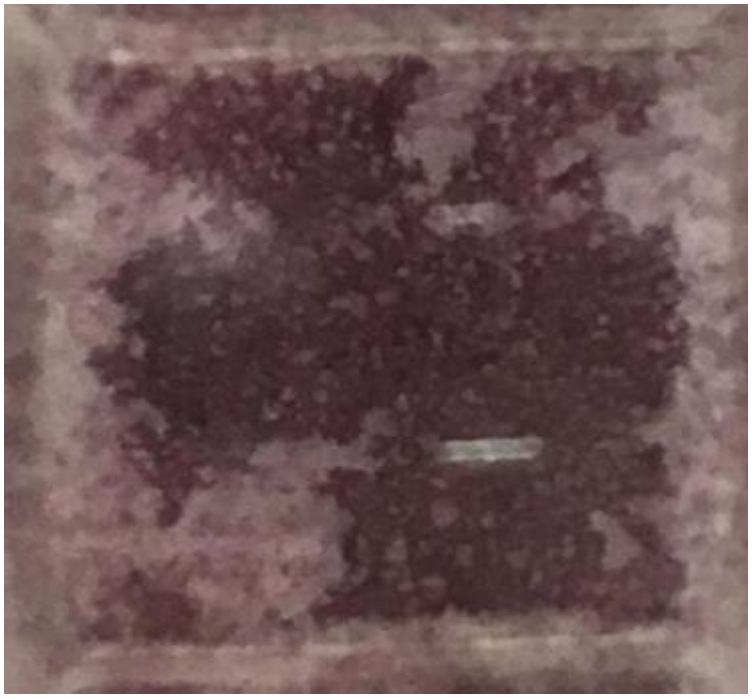

Figure 4.24: Sedimented β-mercaptoethanol-AuNP self-assembled aggregates at the base of cuvette

SEM and microscopic images of the two conditions were compared to witness the morphological changes. It was observed that the control SEM aggregates displayed a different morphology compared to the AuNP solution. The former showed short fused extensions as compared to spheroids fused together in the latter. The round aggregates are the gold nanoparticles coming together due to an irreversible coagulative transition caused by the spontaneous fusion of AuNP nanocolloids. Previous XRD studies have shown the remarkable tendency of SH-AuNPs to rapidly form highly ordered three-dimentional superlattices in the order of micrometres.[2] This nanoseparation technique can be utilized in many applications requiring high SERS signal, solid matrices or protein entrapment.

4.3 Conclusions

In summary, four physical variants of CQDs (E160, E200, W160, W200) were synthesized by the hydrothermal carbonization of the bark of *Arjuna terminalia*.

Further, the catalytic growth of AuNPs was enabled by the prepared CQDs acting as both reducing agents and stabilizers. This study provides useful insights into the efficient route for the synthesis of AuNPs using biologically significant functional groups. The understanding of such principles will provide tunability of size, shape and arrangement of AuNPs affecting their physical properties. FTIR and computational analysis confirms that the C-O group plays a major role in the reductive shape-tuning of AuNPs. CQDs carbonized at 160°C endowed better stability to the AuNPs as compared to the ones synthesized at 200°C hydrothermal temperature. Moreover, Au-WCQDs showed lesser stability as compared to Au-ECQDs. Addition of Type-I collagen to the Au-WCQDs increased their stability manifold. For conferring functionality to the AuNPs, β-mercaptoethanol was used as a linker. It was observed that in the presence of ionic strength, it enables spontaneous 'snowing' of the AuNPs. These sedimented AuNP granules can be used in future in applications requiring strong SERS signals. CQD-AuNP conjugates have huge potential in future for uses as dual fluorescent probes, FRET analysis, biophotonics and drug delivery in biological applications. They can also substitute as tools for electronic circuitry, shape-memory alloys and plasmon resonance-based sensors.

4.4 References

[1] S. Zeng, K. Yong, I. Roy, X. Dinh, X. Yu, F. Luan. A Review on Functionalized Gold Nanoparticles for Biosensing Applications, *Plasmonics* **2016**, *5*, 491–506

[2] M. Daniel, D. Astruc. Gold Nanoparticles: Assembly, Supramolecular Chemistry, Quantum-Size-Related Properties, and Applications toward Biology, Catalysis, and Nanotechnology, *Chem. Rev.* **2004**, *104*, 293−346

[3] S. S. Shankar, A. Rai, B. Ankamwar, A. Singh, A. Ahmad, M. Sastry. Biological synthesis of triangular gold nanoprisms, *Nat. Mater*. **2004**, *3*, 482-488.

[4] A. Corma, H. Garcia, *Chem Soc. Rev.* **2008,** *37*, 2096–2126

[5] N. T. K. Thanh, Z. Rosenzweig, *Anal. Chem.* **2002,** *74*, 1624-1628

[6] G. F. Paciotti, L. Myer, D. Weinreich, D. Goia, N. Pavel, R. E. McLaughlin, L. Tamarkin, *Drug Del.* **2004**, *11*, 169–183

[7] J. Lee, M. S. Han, C. A. Mirkin, *Angew. Chem. Int. Ed.* **2007**, *46*, 4093 –4096

[8] S. S. R. Dasary, A. K. Singh, D. Senapati, H. Yu, P. C. Ray, *J. Am. Chem. Soc.* **2009**, *131*, 13806–13812

[9] R. Lévy, U. Shaheen, Y. Cesbron,V. Sée. Gold nanoparticles delivery in mammalian live cells: a critical review, *Nano Rev.* **2010***, 1*, 4889-4907

[10] K. Haume, S. Rosa, S. Grellet, M. A. Śmiałek, K. T. Butterworth, A. V. Solov'yov, K. M. Prise, J. Golding, N. J. Mason. Gold nanoparticles for cancer radiotherapy: a review, *Cancer Nanotechnol*. **2016**, *7*, 1-20

[11] L. Qina, G. Zenga, C. Laia, D. Huanga, P. Xua, C. Zhanga, M. Chenga, X. Liua, S. Liua, B. Lia, H. Yi. ''Gold rush" in modern science: Fabrication strategies and typical advanced applications of gold nanoparticles in sensing, *Coord Chem Rev*. **2018**, *359*, 1–31

[12] C. Wang, C. Yu. Detection of chemical pollutants in water using gold nanoparticles as sensors: a review, *Rev Anal Chem*. **2013**, *32*, 1–14

[13] S. Ahmed, S. Ikram. Synthesis of Gold Nanoparticles using Plant Extract: An Overview, *Nano Res Applic*. **2015**, *1*, 1-5

[14] J. Wang, J. Qiu. A review of carbon dots in biological applications, *J Mater Sci.* **2016**, *51*, 4728–4738

[15] J. Song, L. Zhao, Y. Wang, Y. Xue, Y. Deng, X. Zhao, Q. Li, Carbon Quantum Dots Prepared with Chitosan for Synthesis of CQDs/AuNPs for Iodine Ions Detection, *Nanomat*. **2018**, *8*, 1043-1054

[16] T. Liu, J. X. Dong, S. G. Liu, N. Li, S. M. Lin, Y. Z. Fan, J. L. Lei, H. Q. Luo, N. B. Li. Carbon quantum dots prepared with polyethyleneimine as both reducing agent

and stabilizer for synthesis of Ag/CQDs composite for Hg2+ ions detection, *J Haz Mater*. **2017**, *322*, 430–436

[17] K. Jiang, S. Sun, L. Zhang, Y. Lu, A. Wu, C. Cai, H. Lin, *Ang Chem*. **2015**, *127*, 5450–5453

[18] L. Zhu, Y. Yin, C.-F. Wang, S. Chen, *J Mat. Chem. C*. **2013**, *1*, 4925-4932

[19] D. Shukla, F. P. Pandey, P. Kumari, N. Basu, M. K. Tiwari, J. Lahiri, R. N. Kharwar, A. S. Parmar. Label-Free Fluorometric Detection of Adulterant Malachite Green Using Carbon Dots Derived from the Medicinal Plant Source *Ocimum tenuiflorum*, *ChemistrySelect* 2019, **4**, 4839 –4847

[20] R. Zhang, Y. Liu, L. Yu, Z. Li, S. Sun. Preparation of high-quality biocompatible carbon dots by extraction, with new thoughts on the luminescence mechanisms, *Nanotechnol*. **2013**, *24*, 225601-225608

[21] V. Amendola, R. Pilot, M. Frasconi, O. M. Maragò, M. A. Iatì. Surface plasmon resonance in gold nanoparticles: a review, *J. Phys. Condens. Matter* **2017**, *29*, 203002-203050

[22] Q. Huang, J. Chen, J. Zhao, J. Pan, W. Lei, Z. Zhang. Enhanced Photoluminescence Property for Quantum Dot-Gold Nanoparticle Hybrid, *Nanoscale Res Let*. **2015**, *10,* 400-405

[23] L. E. S. Hoyos, V. Sa´nchez-Mendieta, M. A. Camacho-López, J. Trujillo-Reyes, A. R. Vilchis-Nestor, Plasmonic and fluorescent sensors of metal ions in water based on biogenic gold nanoparticles, *Arabian J. Chem.* **2018** (in press).

[24] M. Grzelczak, J. Pérez-Juste, P. Mulvaney, L. M. Liz-Marzán. Shape control in gold nanoparticle synthesis, *Chem. Soc. Rev.* **2008**, *37*, 1783–1791

[25] T. K. Sau, C. J. Murphy. High-Yield Synthesis of Multiple Shapes of Gold Nanoparticles in Aqueous Solution, *J. Am. Chem. Soc.* **2004**, *126*, 8648-8649

[26] R. Jagannathan, A. S. Parmar, S. Adyanthaya, A. Prabhune, M. Muschol, P. Poddar. In Situ Observation of Antibiotic Mediated Concurrent Growth of Two Distinct Homogeneous Populations of Gold Nanoparticles in Solution Phase, *J. Phys. Chem. C*. **2009**, *113*, 3478–3486

[27] F. Kim, S. Connor, H. Song, T. Kuykendall, P. Yang, Platonic Gold Nanocrystals, *Angew.Chem. Int. Ed.* **2004**, *43*, 3673–3677

[28] M. L. Personick, C. A. Mirkin, Making Sense of the Mayhem behind Shape Control in the Synthesis of Gold Nanoparticles, *J. Am. Chem. Soc.* **2013**, *135*, 18238−18247

[29] P. Hay, W. Wadt, *J. Chem Phys*. **1985**, *82*, 270-283

[30] J. P. Melo, P. L. Rios, P. Povea, C. Morales-Verdejo, M .B. Camarada, *ACS Omega* **2018**, *3*, 7278-7287

[31] N. Khlebtsov, L. Dykman, Biodistribution and toxicity of engineered gold nanoparticles: a review of *in vitro* and *in vivo* studies, *Chem. Soc. Rev.* **2011***, 40*, 1647–1671

[32] Y. Sun, C. Wang, X. Zhang, L. Ren, X. Tian, Shape Dependence of Gold Nanoparticles on *In Vivo* Acute Toxicological Effects and Biodistribution., *J. Nanoscience Nanotechnol.* **2011***, 11*, 1210–1216

[33] H. Wu, X. Huang, M. Gao, X. Liao, B. Shi, Polyphenol-grafted collagen fiber as reductant and stabilizer for one-step synthesis of size-controlled gold nanoparticles and their catalytic application to 4-nitrophenol reduction, *Green Chem.* **2011***, 13*, 651-658

[34] E. Priyadarshini, N. Pradhan, *Sens Actuators B* **2017**, *238*, 888–902

[35] R. Elghanian, J. J. Storhoff, R. C. Mucic, R. L. Letsinger, C. A. Mirkin, *Science.* **1997***, 277*, 1078 -1081

[36] L. M. Demers, C. A. Mirkin, R. C. Mucic, R. A. Reynolds, R. L. Letsinger, R. Elghanian, G. Viswanadham, *Anal. Chem.* **2000***, 72*, 5535-5541

[37] L. Tang, X. Wang, B. Guo, M. Ma, B. Chen, S. Zhanb, S. Yaoa, *RSC Adv.* **2013***, 3*, 15875–15886